Improvement of 2D finite element analysis stress results by radial basis functions and balance equations

Andrea Chiappa, Corrado Groth, and Marco E. Biancolini

Abstract— This paper presents a method able to upscale finite element (FE) results obtained for coarse meshes of 2D models at a higher resolution, using both radial basis functions (RBF) and balance equations. RBF supply a smooth function from nodal displacements. In addition to FE nodes, RBF interpolation embeds a certain number of additional points, for which displacements satisfy a minimization procedure of the error on balance equations. Derived fields (strain, stress) yield analytically from the constructed interpolator. We tested the method with two 2D structural cases where strong stress concentrations were included. As regards the stress field, an error reduction with respect to validated test benches was observed in all cases.

Keywords— Balance equations, FEM upscaling, meshless, radial basis functions.

I. INTRODUCTION

NOWADAYS finite element method (FEM) plays a major role in solving problems of engineering and mathematical physics [1]. From a general point of view, a complex domain is discretized into a large number of elements. A set of shape functions describes the field of interest inside each element, taking as input its values at the nodes. Although shape functions are the key to treat a unique large domain as a set of smaller and simpler sub-domains, in many cases, they have some important limitations. Often, sufficient requirements for shape functions are the C0 continuity and the patch test. In the structural field, the first condition entails that at element boundaries, only displacements are definitely continuous, whereas stresses are not. Consequently, h-convergence is faster for displacements rather than for stresses [2]. Notoriously, the underlying principle of all structural FEM frameworks is the energetic equivalence of external and internal work. This last is the result of a (numerical) integration over the domain, which requires a computational grid to keep into account the complex shapes of realistic models. Mesh generation is a cumbersome task, especially if complicated geometries are

involved, demanding a considerable portion of the overall computational time [3]. This problem further exacerbates when extremely large deformations occur in the model [4] or when moving discontinuities are under study [5], needing for several mesh updates during the computation. Meshless methods [6] emerged as an attempt to overcome the shortcomings of element-based shape functions and the computational burden of the numerical grid. The basic idea behind meshless methods is to construct the approximation entirely in terms of nodes.

One of the first meshless methods is the smooth particle hydrodynamics (SPH) method by Lucy [7]. This approach was used to study a protostar as a finite set of interacting points simulating gas particles. Later on, Libersky *et al.* [8] employed the same method in the dynamics of elastic-plastic solids, where its meshless characteristic well suited large distortions.

Nayroles *et al.* [9] were the first to introduce the so-called diffused approximation (DA). This method assigns at each point of the set a circumscribed interpolating function whose coefficients minimize a properly defined L2 norm. In such a way, the boundaries of each local interpolation assume a fuzzy characteristic, enhancing continuity with respect to traditional basis functions. Belytscho and co-workers [10] coupled the DA with the Galerkin method. Although a grid is still present to carry out numerical quadrature, it is independent of the model geometry. The partition of unity method (POU) [11] is similar under some aspects to the DA (overlapping patches covering the whole domain), anyway the possibility to include the differential expression of the problem in the local approximation space and its differentiability *ad libitum* constitute innovative features. Another class of meshless approaches relies on local weak forms, such as the local Petrov-Galerkin method [12]. This procedure prescribes the subdivision of the global domain into regular overlapping subdomains, in which integration evaluates in a truly meshless fashion.

Radial basis functions (RBF) were introduced to deal with problems of multidimensional interpolation [13]. In [14] Kansa proposed the so-called collocation method based on multiquadratics (MQ) RBF to obtain approximate solutions to partial differential equations (PDEs) problems. The derivability and accuracy of MQ allow the construction of large systems of equations, where a function and its derivatives

A. Chiappa is with the University "Tor Vergata", Rome, Viale del Politecnico, 1, 00133, Italy (phone: (+39) 06-72597136; e-mail: andrea.chiappa@uniroma2.it).

C. Groth is with the University "Tor Vergata", Rome, Viale del Politecnico, 1, 00133, Italy (e-mail: corrado.groth@uniroma2.it).

M. E. Biancolini is with the University "Tor Vergata", Rome, Viale del Politecnico, 1, 00133, Italy (e-mail: biancolini@ing.uniroma2.it).

appear all at once. This method showed its efficacy in a variety of applications, involving both global [15]-[17] and local [18]-[20] RBF. Despite its versatility, Fasshauer [21] pointed out drawbacks of this strategy such as the asymmetry of the associated matrix and its singularity for certain arrangements of points, proposing a Hermitian form able to overcome these issues.

Collocation methods are not the only way to adopt RBF in a meshless solution process. The method of fundamental solutions (MFS) [22] as well as the dual reciprocity method (DRM) [23] can adopt RBF to handle various problems, with no mesh involved. In [24] and [25] RBF substitute classical shape functions for the local approximation task while a background mesh is still necessary to integrate the Galerkin weak form.

The authors recently proposed a method to improve FEM results obtained for 2D models [26]. As previously mentioned, FEM displacements are continuous across elements and exhibit a faster h-convergence with respect to their derived fields. RBF interpolation of FEM displacements provides a continuous analytical form over the domain. Strain and stress fields obtained from derivation of the RBF interpolator do not suffer from the continuity problems typical of shape functions, showing a higher accuracy with respect to FEM. The proposed method proved to give the greatest benefit when coarse meshes are considered, improving FEM results in correspondence of stress raisers. In this paper, we move a step forward from that achievement. RBF still provide an analytical and differentiable form to the scattered displacements obtained with FEM. Unlike in [26], the sought improvement does not rely only on the enhanced continuity of RBF interpolation, but also on the reduction of local imbalance. For this purpose, spare points are added to FEM nodes. Additional values of displacement are determined minimizing the vector norm of the pointwise deviations from local balance, while keeping FEM values at the original nodes. Once the displacement field embeds local balance, strain and stress states are retrieved. In many cases encountered in literature, PDEs are the starting point for the construction of weak forms, often requiring a grid for the integration over the domain. The present work supplies a post-processing method for FEM results, exploiting the analytical differentiability of a RBF support, without involving the mesh.

II. RADIAL BASIS FUNCTIONS

Radial basis functions interpolation is a subject covered in many dedicated textbooks, from either a mere mathematical [27] or a more applicative perspective [28]. RBF have given their contribution in a wide range of fields pertaining to engineering and science: neural networks [29] to computer graphics (surface reconstruction [30]), mesh morphing [31]-[32] to image analysis of deformations [33] and data transfer [34]. RBF mesh morphing has been employed for several applications, from FSI coupling [35] to genetic [36], evolutionary optimizations [37] and advanced modelling [38].

Let suppose to have a set of N points x_i with $i=1,\dots,N$ in $\mathbb{R}^d$

for which the scalar values g_i are assigned. A RBF interpolant $s(x)$ is a series of radial basis φ, biased by the weights γ_i:

$$s(\mathbf{x}) = \sum_{i=1}^{N} \gamma_i \varphi\left(\|\mathbf{x} \cdot \mathbf{x_i}\|\right) \tag{1}$$

Two significant benefits of RBF interpolation are clear from the above expression:
1) Interpolation is constructed just in terms of nodes.
2) The Euclidean norm reduces the original space dimension to a scalar quantity, providing dimensional independence.

Typical RBF kernels are shown in Table 1 with $r = \|\mathbf{x} \cdot \mathbf{x_i}\|$, ϵ is a shape parameter [39], which should depend upon the average grid spacing. Given the expressions in Table 1, it is worth to notice that the generalized multiquadratic can assume also the form of any spline, multiquadratic, inverse multiquadratic and inverse quadratic kernel with a proper choice of the exponent q and of the parameter R.

The coefficients γ_i are such that the interpolator $s(x)$ gives exactly the values g_i at the original (source) points x_i. In matrix form:

$$\mathbf{M\gamma = g} \tag{2}$$

The matrix M collects the radial basis φ computed at the source points and its inversion is necessary to determine the vector of weights γ. Sometimes it is convenient to add a polynomial supplement $h(x)$ to the expression in (1), in this way polynomial functions of the same form of $h(x)$ can be reproduced exactly. This comes at the cost of a formal complication of the system in (2), anyway in the present work we make no use of the polynomial supplement thus no more details are given in this regard.

It seems suitable to continue this brief dissertation on RBF, rather general so far, directly addressing the workflow presented in this paper. In the specific context, RBF reproduce two-dimensional displacement fields. Thus, it is appropriate to illustrate the case of RBF interpolating a vector field in 2D. As the RBF interpolation works on scalar functions, each component of the displacement field requires its RBF series:

$$\begin{cases} u = s_x(\mathbf{x}) = \sum_{i=1}^{N} \gamma_i^x \varphi\left(\|\mathbf{x} - \mathbf{x_i}\|\right) \\ v = s_y(\mathbf{x}) = \sum_{i=1}^{N} \gamma_i^y \varphi\left(\|\mathbf{x} - \mathbf{x_i}\|\right) \end{cases} \tag{3}$$

Strain is the symmetric part of the gradient of the vector field of (3) and is the result of a differentiation procedure. Radial basis are derived with respect to x and y. Taking the example of the GMQ kernel, it is straightforward to apply the chain rule which yields

$$\frac{\partial s(\mathbf{x})}{\partial x} = \sum_{i=1}^{N} \gamma_i \cdot q\left(\epsilon^2 r^2 + R^2\right)^{q-1} 2\epsilon^2 (x - x_i)$$

$$\frac{\partial s(\mathbf{x})}{\partial y} = \sum_{i=1}^{N} \gamma_i \cdot q\left(\epsilon^2 r^2 + R^2\right)^{q-1} 2\epsilon^2 (y - y_i) \tag{4}$$

The differentiation procedure recurs as many times as the degree of derivative required. Differential equations of balance contain second degree derivatives of the components of

displacement, thus the differentiation rule must be repeated twice.

Table 1 most common radial basis functions

RBF	$\varphi(r)$
Spline type (Rn)	r^n, n odd
Thin plate spline (TPSn)	$r^n \log(r)$, n even
Multiquadratic (MQ)	$\sqrt{1+\epsilon^2 r^2}$
Inverse multiquadratic (IMQ)	$\dfrac{1}{\sqrt{1+\epsilon^2 r^2}}$
Inverse quadratic (IQ)	$\dfrac{1}{1+\epsilon^2 r^2}$
Gaussian (GS)	$e^{-\epsilon^2 r^2}$
Generalized multiquadratic (GMQ)	$(\epsilon^2 r^2 + R^2)^q$

III. NUMERICAL PROCEDURE

This paper presents a progress with respect to the former work detailed in [26]. For sake of completeness, the following points outline the referenced method:
1) Several 2D structural cases of stress concentration were solved via FEM.
2) RBF interpolation supplied a smooth form of the displacement field, starting from FEM nodal values.
3) Analytical differentiation of the interpolated displacements provided the strain field.
4) Application of Hook's law supplied the stress map throughout the model, which proved to be more accurate than that provided by FEM for the same case.

The mentioned paper also showed the convergence of the method when increasing the level of mesh refinement up to a very dense discretization.

The progress developed here consists in including local balance in the RBF interpolator. As in [26], we still consider two-dimensional plane stress problems. The material is homogeneous and isotropic. Under these assumptions, Hook's law relates stress to strain vector as follows:

$$\begin{Bmatrix} \sigma_x \\ \sigma_y \\ \tau_{xy} \end{Bmatrix} = \begin{bmatrix} \dfrac{E}{1-v^2} & \dfrac{vE}{1-v^2} & 0 \\ \dfrac{vE}{1-v^2} & \dfrac{E}{1-v^2} & 0 \\ 0 & 0 & G \end{bmatrix} \begin{Bmatrix} \varepsilon_x \\ \varepsilon_y \\ \varepsilon_{xy} \end{Bmatrix} \quad (5)$$

where E is the Young modulus, v is the Poisson coefficient and the shear modulus is

$$G = \frac{E}{2(1+v)} \quad (6)$$

Displacement derivatives form the strain components:

$$\varepsilon_x = \frac{\partial u}{\partial x}$$
$$\varepsilon_y = \frac{\partial v}{\partial y} \quad (7)$$
$$\varepsilon_{xy} = \frac{\partial u}{\partial y} + \frac{\partial v}{\partial x}$$

Stresses inside the material should satisfy equilibrium equations, with no body force applied and for 2D plane stress cases, they assume the form:

$$\frac{\partial \sigma_x}{\partial x} + \frac{\partial \tau_{xy}}{\partial y} = 0$$
$$\frac{\partial \tau_{xy}}{\partial x} + \frac{\partial \sigma_y}{\partial y} = 0 \quad (8)$$

Plugging (5)-(7) in (8), equilibrium equations can be written in terms of displacement derivatives:

$$\frac{1}{1-v}\left(\frac{\partial^2 u}{\partial x^2} + v\frac{\partial^2 v}{\partial x \partial y}\right) + \frac{1}{2}\left(\frac{\partial^2 u}{\partial y^2} + \frac{\partial^2 v}{\partial x \partial y}\right) = 0$$
$$\frac{1}{2}\left(\frac{\partial^2 u}{\partial x \partial y} + \frac{\partial^2 v}{\partial x^2}\right) + \frac{1}{1-v}\left(\frac{\partial^2 v}{\partial y^2} + v\frac{\partial^2 u}{\partial x \partial y}\right) = 0 \quad (9)$$

RBF interpolation provides u and v in a continuous and differentiable form. Coefficients vectors $\boldsymbol{\gamma}^x$ and $\boldsymbol{\gamma}^y$ allow expressing the components of displacement as RBF series (see (3)). They come from the inverse problems:

$$\boldsymbol{\gamma}^x = \mathbf{M}^{-1}\mathbf{u}$$
$$\boldsymbol{\gamma}^y = \mathbf{M}^{-1}\mathbf{v} \quad (10)$$

Vectors $\boldsymbol{u}$ and $\boldsymbol{v}$ contain the scattered data from which interpolation starts. The aim of the proposed method is to embed local balance in the series form of (3), retaining nodal displacements. Bearing this in mind, global vectors must contain displacements both at FEM nodes and in correspondence of new sites, whose associated values minimize error on balance. Let N_F and N_a be the number of FEM nodes and added points respectively, we pose

$$\mathbf{u} = \mathbf{u_0} + \mathbf{S}\mathbf{u_a}$$
$$\mathbf{v} = \mathbf{v_0} + \mathbf{S}\mathbf{v_a} \quad (11)$$

The row-vectors $\boldsymbol{u_0}$ and $\boldsymbol{v_0}$ have dimension N_F+N_a, with FEM nodal displacements in the first N_F positions and zero afterwards. The vectors $\boldsymbol{u_a}$ and $\boldsymbol{v_a}$ contain the N_a values of displacement at additional points. The matrix $\boldsymbol{S}$ concatenates displacements in order to assemble the global vectors. It consists of two sub-matrices:

$$\mathbf{S} = \begin{bmatrix} \mathbf{0} \\ \mathbf{I} \end{bmatrix} \quad (12)$$

The matrix $\boldsymbol{0}$ is all-zeros $N_F \times N_a$, $\boldsymbol{I}$ is the identity matrix with dimension $N_a \times N_a$. Plugging (11) in (10) we obtain

$$\boldsymbol{\gamma}^x = \mathbf{M}^{-1}\mathbf{u_0} + \mathbf{M}^{-1}\mathbf{S}\mathbf{u_a}$$
$$\boldsymbol{\gamma}^y = \mathbf{M}^{-1}\mathbf{v_0} + \mathbf{M}^{-1}\mathbf{S}\mathbf{v_a} \quad (13)$$

RBF interpolation supplies the displacement field in a smooth form, for which derivation only acts on the matrix $\boldsymbol{M}$ of radial basis. The notations ∂M and $\partial^2 M$ adopted below

indicate the matrices containing the first and second order derivatives of the terms in $\mathbf{M}$, computed at all the points of the system (i.e. FEM nodes and additional sites). We state the following equalities

$$\mathbf{q_x} = \frac{1}{1-\nu}\left(\frac{\partial^2 \mathbf{M}}{\partial x^2}\mathbf{M^{-1}u_0} + \nu\frac{\partial^2 \mathbf{M}}{\partial x \partial y}\mathbf{M^{-1}v_0}\right)$$
$$+\frac{1}{2}\left(\frac{\partial^2 \mathbf{M}}{\partial y^2}\mathbf{M^{-1}u_0} + \frac{\partial^2 \mathbf{M}}{\partial x \partial y}\mathbf{M^{-1}v_0}\right), \quad (14)$$

$$\mathbf{q_y} = \frac{1}{2}\left(\frac{\partial^2 \mathbf{M}}{\partial x \partial y}\mathbf{M^{-1}u_0} + \frac{\partial^2 \mathbf{M}}{\partial x^2}\mathbf{M^{-1}v_0}\right)$$
$$+\frac{1}{1-\nu}\left(\frac{\partial^2 \mathbf{M}}{\partial y^2}\mathbf{M^{-1}v_0} + \nu\frac{\partial^2 \mathbf{M}}{\partial x \partial y}\mathbf{M^{-1}u_0}\right), \quad (15)$$

$$\mathbf{R_x} = \frac{1}{1-\nu}\frac{\partial^2 \mathbf{M}}{\partial x^2}\mathbf{M^{-1}S} + \frac{1}{2}\frac{\partial^2 \mathbf{M}}{\partial y^2}\mathbf{M^{-1}S}, \quad (16)$$

$$\mathbf{R_y} = \frac{1}{2}\frac{\partial^2 \mathbf{M}}{\partial x^2}\mathbf{M^{-1}S} + \frac{1}{1-\nu}\frac{\partial^2 \mathbf{M}}{\partial y^2}\mathbf{M^{-1}S}, \quad (17)$$

$$\mathbf{T} = \frac{1}{2}\frac{\partial^2 \mathbf{M}}{\partial x \partial y}\mathbf{M^{-1}S} + \frac{1}{1-\nu}\frac{\partial^2 \mathbf{M}}{\partial x \partial y}\mathbf{M^{-1}S}. \quad (18)$$

Using (14)-(18), residuals of balance equations (9) assume the compact form

$$\mathbf{e_x} = \mathbf{R_x u_a} + \mathbf{T v_a} + \mathbf{q_x}$$
$$\mathbf{e_y} = \mathbf{R_y v_a} + \mathbf{T u_a} + \mathbf{q_y} \quad (19)$$

We consider the sum of the squared norms of $\mathbf{e_x}$ and $\mathbf{e_y}$ as a measure of the overall error on balance e:

$$\|\mathbf{e_x}\|^2 = \left(\mathbf{R_x u_a} + \mathbf{T v_a} + \mathbf{q_x}\right)^T\left(\mathbf{R_x u_a} + \mathbf{T v_a} + \mathbf{q_x}\right)$$
$$\|\mathbf{e_y}\|^2 = \left(\mathbf{R_y v_a} + \mathbf{T u_a} + \mathbf{q_y}\right)^T\left(\mathbf{R_y v_a} + \mathbf{T u_a} + \mathbf{q_y}\right), \quad (20)$$

$$e = \|\mathbf{e_x}\|^2 + \|\mathbf{e_y}\|^2. \quad (21)$$

Sought vectors $\mathbf{u_a}$ and $\mathbf{v_a}$ are those that minimize e:

$$\begin{cases} \dfrac{\partial e}{\partial \mathbf{u_a}} = \mathbf{0} \\[2mm] \dfrac{\partial e}{\partial \mathbf{v_a}} = \mathbf{0} \end{cases} \quad (22)$$

For sake on conciseness, we adopt

$$\mathbf{p_x} = -\left(\mathbf{R_x}^T\mathbf{q_x} + \mathbf{T}^T\mathbf{q_y}\right), \quad (23)$$

$$\mathbf{p_y} = -\left(\mathbf{R_y}^T\mathbf{q_y} + \mathbf{T}^T\mathbf{q_x}\right), \quad (24)$$

$$\mathbf{Q_x} = \mathbf{R_x}^T\mathbf{R_x} + \mathbf{T}^T\mathbf{T}, \quad (25)$$

$$\mathbf{Q_y} = \mathbf{R_y}^T\mathbf{R_y} + \mathbf{T}^T\mathbf{T}, \quad (26)$$

$$\mathbf{D_x} = -\left(\mathbf{R_x}^T\mathbf{T} + \mathbf{T}^T\mathbf{R_y}\right), \quad (27)$$

$$\mathbf{D_y} = -\left(\mathbf{R_y}^T\mathbf{T} + \mathbf{T}^T\mathbf{R_x}\right). \quad (28)$$

Equations (23)-(28) allow to express $\mathbf{u_a}$ and $\mathbf{v_a}$ in the short form

$$\mathbf{u_a} = \left(\mathbf{Q_x} - \mathbf{D_x Q_y^{-1} D_y}\right)^{-1}\left(\mathbf{D_x Q_y^{-1} p_y} + \mathbf{p_x}\right),$$
$$\mathbf{v_a} = \left(\mathbf{Q_y} - \mathbf{D_y Q_x^{-1} D_x}\right)^{-1}\left(\mathbf{D_y Q_x^{-1} p_x} + \mathbf{p_y}\right). \quad (29)$$

It is worth to notice that the matrices $\mathbf{Q_x}$ and $\mathbf{Q_y}$ and their inverse forms are symmetric, given (25) and (26). Since $\mathbf{D_x}^T = \mathbf{D_y}$, as deducible from (27) and (28), also the matrices $\left(\mathbf{Q_x} - \mathbf{D_x Q_y^{-1} D_y}\right)$ and $\left(\mathbf{Q_y} - \mathbf{D_y Q_x^{-1} D_x}\right)$ are symmetric. Tailored algorithms exist for the inversion of symmetric matrices, which allow the process to run in a relatively short time.

IV. NUMERICAL TESTS

Two plane cases of structures with a strong stress concentration supply a robust test bench for the proposed method: a plate with a single hole in traction and a planar structure under compression with three holes drilled. Literature supplies a theoretical result for the first instance. For both geometries, a series of FEM analyses allowed to test the convergence up to a very fine mesh considered as golden standard (GS). FEM results obtained for the GS supply a benchmark for the second case, providing for the lack of referenced data. The mesh size is controlled by the number of elements along a quarter of the hole circumference. In [26] the upscaling of FEM results occurred thanks to the enhanced continuity of the RBF interpolator. Here, the process is controllable with the number of spare points and it relies on local balance, further than on the favourable mathematical properties of RBF. The adopted kernel for both methods relying on RBF is the generalized multiquadratics (GMQ) with $q = 1.5$, $R = 0.1$, $\epsilon = 1$ for the plate and $\epsilon = 0.1$ for the rib. The FEM framework used to produce numerical results is Ansys APDL.

FEM results for the GS are compared with the ones obtained with the proposed method. The quality of the output is verified both locally and globally. A first comparison regarded the peak stress, in correspondence of the stress raiser. As a second step, global matching is taken into account. For this last assessment, stress evaluation at the nodes of the GS mesh proceeded employing the proposed method. In this way, the point-wise difference with the GS FEM value gives an error for each stress component. The L2 norm of the vector containing all these quantities is normalized on the L2 norm of the vector with GS nodal stresses, to measure the global error. The same procedure holds to compute the global error also for the RBF method described in [26] and when original FEM stresses are interpolated at GS nodes by means of shape functions.

Addition of spare points follows a systematic workflow, which makes use of Delaunay triangulation. Triangular patches are built using pre-existing nodes, additional spare points are the mid-side nodes of the last generated triangles. This process can be iterated several times starting from FEM nodes to produce the desired level of density, without the risk of generating coincident points. In the remainder of the paper, the number of iterations of the above-described procedure indicates the amount of additional points introduced to enhance local balance, increasing from 1 to 4. Higher densities

lead to the ill conditioning of the matrices containing Euclidean correlations.

A strong advantage of the method is that the addition of spare points can affect only critical areas, like the ones hosting stress concentrations, with a wise usage of computational resources.

A. Hole in a plate under traction

This case is the same first analysed in [26], for sake of completeness dimensions are reported below:

- B = base = 30 mm
- H = height = 15 mm
- d = diameter of the hole = 10 mm

The nominal tensile stress is 1000 MPa, which is the traction applied at the boundary. The geometry has two axes of symmetry, which allows the numerical model to be just a quarter of the whole structure, given proper constraints at the boundaries (Fig. 1). Three-noded triangular elements were used (SHELL41) with stiffness only on the plane of definition and unitary thickness. The theoretical stress concentration factor is available in literature [40], [41] and, given the above dimensions it is equal to 3.471. X-component of the stress (σ_x) was used in calculating the stress concentration factor. The area in which additional points are introduced is restrained at a radius of 10 mm around the hole centre.
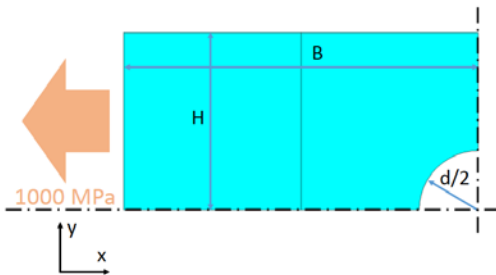
Fig. 1 APDL case geometry for the plate with one centred hole

B. Wing rib with three lightening holes under compressive load

The second case addressed is a flat wing rib with three lightening holes drilled [26], [42]. Also in this case it is possible to take advantage of the double symmetry of the structure, reducing the extension of the numerical counterpart. The dimensions of the model are

- H1 = 196.5 mm, height of the left edge and of module 1 and 2
- H2 = 229.5 mm, height of the right edge
- d = 200 mm, diameter of the holes
- B1 = 393 mm, base of module 1, two times the base of module 2
- B2 = 627 mm, base of the model

A dimensioned sketch of the rib is in Fig. 2.

SHELL41, 4-noded quadrilateral elements with unitary thickness were deployed for the discretization of the model. The rib is subject to a compressive load of 100 MPa, acting along the curved edge. FEM results for the GS serve as reference, since no theoretical data are available for this case.

In Fig. 3 the coloured map obtained for the GS is visible, showing the x-component of the stress (σ_x). The RBF post-processing method is applied to both module 1 and module 2 (highlighted in Fig. 2), including stress raisers of different severities. The stress component considered for the peaks is σ_x at the holes top, its values are 219.3 MPa and 74.8 MPa for the side and central hole respectively. The areas concerned with point addition are the circular belts around the holes, with external radius 150 mm.
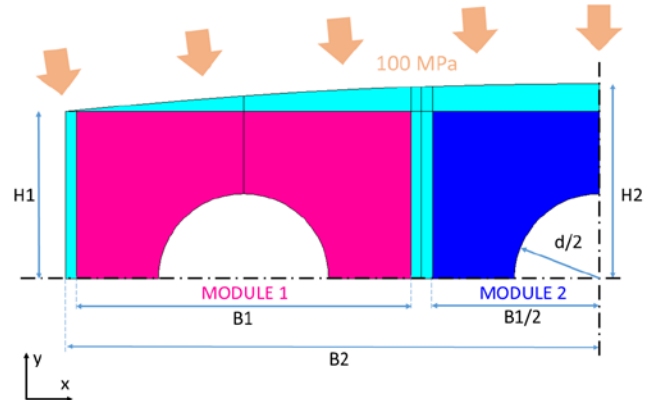
Fig. 2 APDL case geometry for the rib with three lightening holes
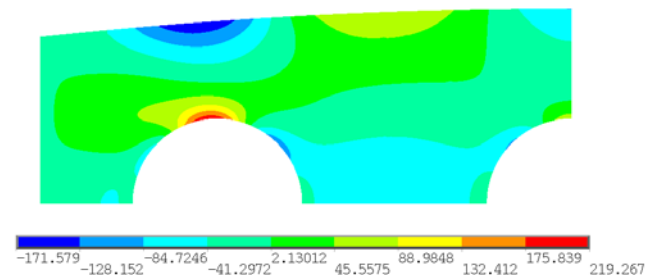
Fig. 3 stress level curves for σ_x obtained by the FEM model for the rib with three lightening holes

V. RESULTS AND DISCUSSION

We used meshes with an increasing level of refinement to retrieve FEM data necessary to run the method. The procedure is assessed considering both the ability to capture the stress peak and considering the global accuracy of the full stress field.

A. Stress peak estimation

The stress peaks for the two methods relying on RBF are detected interpolating at the GS grid nodes of the portion analysed. The case considered first is the plate with a hole in traction. Table 2 summarizes relevant results. The first column from left reports the level of discretization of the starting mesh given as the number of subdivisions along a quarter of the hole. Stress concentration factors retrieved from FEM analysis and with the RBF method exposed in [26] appear in the second and third columns respectively. The fourth, fifth, sixth and seventh columns collect the stress concentration factors found with the proposed strategy for a growing amount of spare

points. The procedure adopting RBF and local balance (LB) exhibits its greatest accuracy if enough spare points (3 iterations) are included. A further increase of spare points proved detrimental (4 iterations). Considering the case of 3 iterations, results are very close to those of RBF without LB. In particular, only for 4 and 10 subdivisions of the hole edge, a slight improvement is observed. In Fig. 4, APDL mesh of the plate with four subdivisions of the hole edge is shown with additional points (in red), after 3 iterations of Delaunay triangulation.

The wing rib contains two different stress raisers, in correspondence of the holes located at the left and at the centre of the model. Two distinct applications of the method took place for module 1 and 2. Results are reported in Table 3 and Table 4, for module 1 and 2 respectively. As regards module 1, the best match of RBF + LB with the benchmark occurs for the case of 2 iterations. Only for two (4 and 6 subdivisions) of the four considered cases the stress peak is captured more precisely than with RBF [26], anyway the gain in precision is rather limited. As concerns module 2, results approach closer to the reference when the largest amount of additional points (4 iterations) is employed. In this case, a tangible advantage with respect to RBF [26] is observable.

Both methods involving RBF captured the stress peak with a greater accuracy if compared to the FEM model supplying nodal displacements, for all the considered instances.
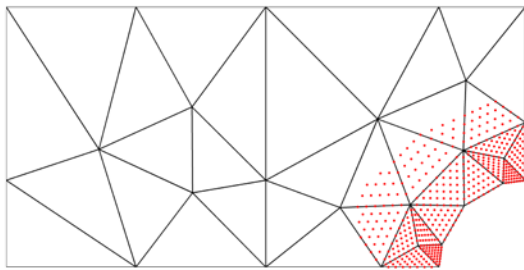
Fig. 4 APDL mesh for the plate in traction with 4 subdivisions of the hole edge. Additional points obtained with 3 iterations of Delaunay triangulation are visible in red

B. Global error evaluation

The application of the method involving RBF + LB leads to an evolution of the stress contour affecting a certain area, it seemed relevant to investigate the quality of the modified stress field with respect to a reference, throughout the whole portion considered. Table 5 refers to the plate with a hole in traction. Table 6 reports the results for module 1 of the drilled rib, Table 7 exposes the results for module 2 in the same way. The first column from left reports the level of discretization as before, the second and third columns list the percentage errors with respect to GS for FEM interpolation of stresses (by means of shape functions) and for the RBF method. The case of RBF + LB is shown from column four to six, depending on the amount of additional points. For all the analysed instances,

RBF + LB proved effective in reducing the global error with respect to concurrent methods, even if its action is restricted to a limited portion around the holes. The best outcome occurs with an amount of additional points given by 3 iterations for almost all the cases. Fig. 5 reports a comparison of stress maps for σ_x against the GS (c). In a), σ_x obtained with APDL for the model with 4 divisions of the hole edge is interpolated at the nodes of the GS mesh by means of triangular shape functions. b) and d) show σ_x maps as output of RBF and RBF + LB methods respectively. In Fig. 6 the same comparison involves module 2 of the wing rib. FEM coarse mesh used as input featured 10 subdivisions of the hole edge. In both cases, introduction of LB trimmed stress contours in correspondence of the holes more similar to GS than when RBF work alone.

It is interesting to notice that it does not appear a strict correspondence between global and local accuracy in terms of stress peak, since they are often met under different circumstances.

The proposed procedure combining RBF and balance equations achieved the lowest global errors for all the considered examples.

Matrix inversions for the methods based on RBF are performed thanks to the tool embedded in the MATLAB Arithmetic Package, which exploits the Cholesky decomposition or the LDL decomposition, a closely related variant of the classical Cholesky decomposition. For sake of completeness, Table 8 reports the running times measured for the module 2 of the wing rib, relative to the application of the methods involving RBF interpolation.

VI. CONCLUSION

This paper exposes a numerical method combining RBF interpolation and local balance equations. The method takes as input the output displacements of a FEM structural analysis performed with a coarse mesh, its purpose is to derive a stress field of enhanced accuracy with respect to the FEM model used as input. To account for the extra information on local balance, additional 'spare' points are added to FEM nodes, the new values of displacements are those minimizing the imbalance at the points constituting the system. Two instances of structures exhibiting strong stress concentrations allowed to show the effectiveness of the proposed strategy, whose performance was tested both at local and global scales. Literature along with finely discretized FEM models supplied data to assess the method. As regards the stress peak detection, the proposed workflow always achieved a benefit with respect to the starting FEM model, but only in some cases with respect to the strategy in [26], also taken as term of comparison. The lowest global error was met by the presented method for all the considered examples. A point left open regards the *a priori* knowledge of the amount of additional points leading to the best outcome, since their indiscriminate increase often proved detrimental already before ill conditioning occurs.
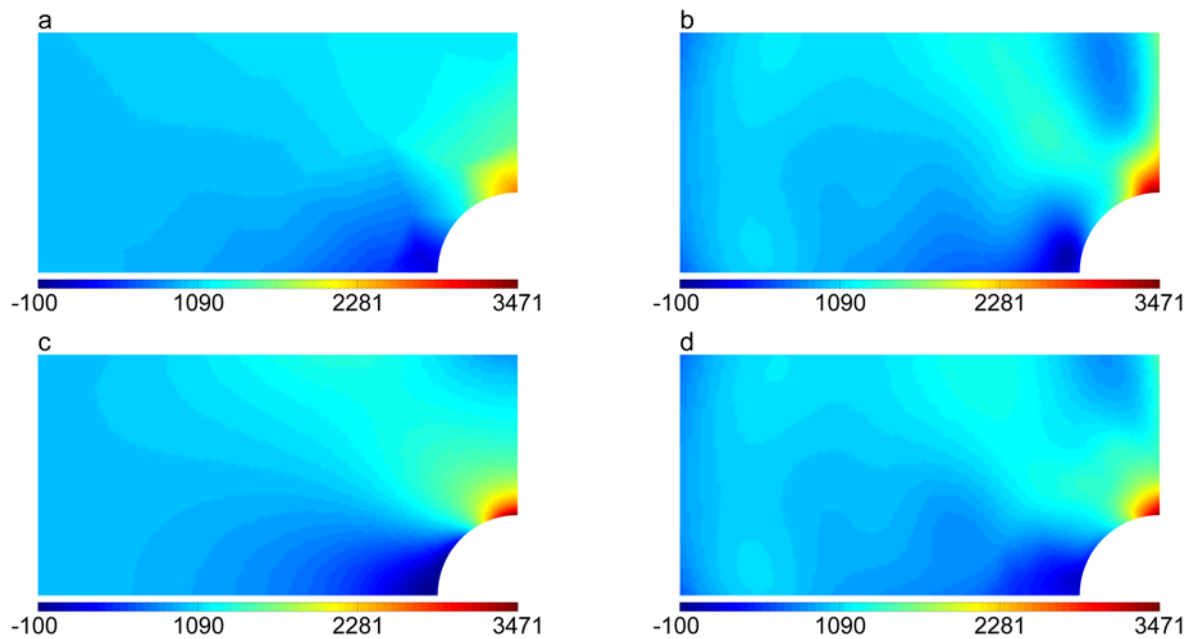
Fig. 5 stress level curves of σ_x for the plate with one centred hole. a) σ_x obtained with FEM for 4 subdivision of the hole edge is interpolated at GS nodes using triangular shape functions. b) σ_x obtained with RBF, input displacements are from the model with 4 subdivisions of the hole edge. c) σ_x obtained with FEM for the GS mesh. d) σ_x obtained with RBF + LB. Input data are the same of b. Three iterations of Delaunay triangulation occurred for points augmentation
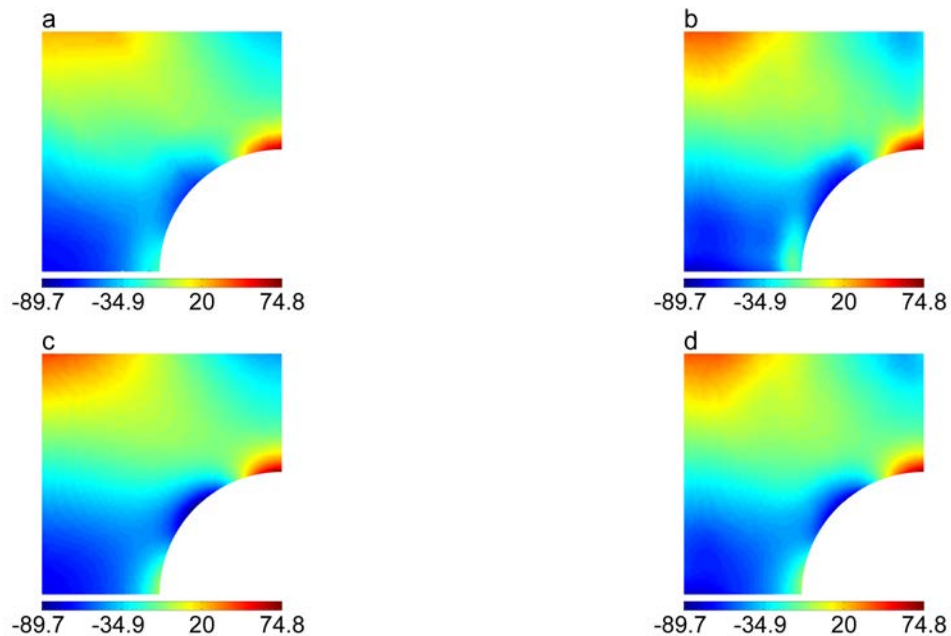
Fig. 6 stress level curves of σ_x for module 2 of the wing rib. a) σ_x obtained with FEM for 10 subdivision of the hole edge is interpolated at GS nodes using iso-parametric shape functions. b) σ_x obtained with RBF, input displacements are from the model with 10 subdivisions of the hole edge. c) σ_x obtained with FEM for the GS mesh. d) σ_x obtained with RBF + LB. Input data are the same of b. Three iterations of Delaunay triangulation occurred for points augmentation

Table 2 plate with a hole in traction. Evaluation of the stress concentration factor

Subdivisions of the hole edge	K_t APDL	K_t RBF	K_t RBF+LB 1 iter	K_t RBF+LB 2 iter	K_t RBF+LB 3 iter	K_t RBF+LB 4 iter
4	2.572	3.356	3.270	3.311	3.446	3.614
6	2.801	3.201	3.106	3.105	3.174	3.156
8	3.203	3.453	3.400	3.420	3.442	3.399
10	3.279	3.499	3.427	3.429	3.458	3.316

Table 3 wing rib, module 1. Evaluation of the stress peak

Subdivisions of the hole edge	$\sigma_{x,max}$ [MPa] APDL	$\sigma_{x,max}$ [MPa] RBF	$\sigma_{x,max}$ [MPa] RBF+LB 1 iter	$\sigma_{x,max}$ [MPa] RBF+LB 2 iter	$\sigma_{x,max}$ [MPa] RBF+LB 3 iter	$\sigma_{x,max}$ [MPa] RBF+LB 4 iter
4	160.7	185.5	185.8	188.7	187.1	185.8
6	181.9	200.6	201.9	201.7	199.8	198.9
8	199.6	209.2	209.0	207.6	206.5	204.8
10	207.2	213.8	212.4	210.7	210.1	201.1

Table 4 wing rib, module 2. Evaluation of the stress peak

Subdivisions of the hole edge	$\sigma_{x,max}$ [MPa] APDL	$\sigma_{x,max}$ [MPa] RBF	$\sigma_{x,max}$ [MPa] RBF+LB 1 iter	$\sigma_{x,max}$ [MPa] RBF+LB 2 iter	$\sigma_{x,max}$ [MPa] RBF+LB 3 iter	$\sigma_{x,max}$ [MPa] RBF+LB 4 iter
4	43.2	43.2	45.7	48.0	56.0	63.7
6	57.6	57.5	60.9	62.9	67.4	69.6
8	64.2	64.4	66.3	68.0	70.7	71.7
10	67.7	68.0	69.3	70.6	72.1	72.7

Table 5 plate with a hole in traction. Global errors

Subdivisions of the hole's edge	L2 error % FEM	L2 error % RBF	L2 error % RBF+LB 1 iter	L2 error % RBF+LB 2 iter	L2 error % RBF+LB 3 iter	L2 error % RBF+LB 4 iter
4	24.60%	24.15%	22.49%	19.87%	19.15%	21.81%
6	21.63%	21.74%	19.18%	16.94%	16.04%	18.93%
8	12.69%	11.38%	10.13%	8.37%	7.81%	10.13%
10	10.90%	9.88%	8.40%	7.21%	7.11%	9.93%

Table 6 wing rib, module 1. Global errors

Subdivisions of the hole's edge	L2 error % FEM	L2 error % RBF	L2 error % RBF+LB 1 iter	L2 error % RBF+LB 2 iter	L2 error % RBF+LB 3 iter	L2 error % RBF+LB 4 iter
4	24.58%	26.61%	21.51%	20.13%	19.73%	20.17%
6	15.48%	14.99%	11.52%	9.56%	9.04%	9.32%
8	11.04%	10.33%	7.82%	6.08%	5.76%	7.37%
10	14.04%	7.52%	5.36%	4.11%	3.99%	14.23%

Table 7 wing rib, module 2. Global errors

Subdivisions of the hole's edge	L2 error % FEM	L2 error % RBF	L2 error % RBF+LB 1 iter	L2 error % RBF+LB 2 iter	L2 error % RBF+LB 3 iter	L2 error % RBF+LB 4 iter
4	20.19%	24.28%	20.11%	19.24%	19.73%	20.40%
6	12.98%	13.76%	9.72%	8.26%	7.87%	8.12%
8	9.14%	8.81%	6.40%	5.18%	4.90%	5.00%
10	7.03%	6.34%	4.40%	3.53%	3.40%	3.67%

Table 8 module 2 of the wing rib, running times for the methods based on RBF

Subdivisions of the hole's edge	Running time [s] RBF	Running time [s] RBF+LB 1 iter	Running time [s] RBF+LB 2 iter	Running time [s] RBF+LB 3 iter	Running time [s] RBF+LB 4 iter
4	0.0402	0.0043	0.0320	0.0588	0.7807
6	0.0407	0.0067	0.0258	0.3131	6.5354
8	0.0409	0.0185	0.0622	1.0462	25.7449
10	0.0388	0.0190	0.1461	2.4133	84.6988

References

[1]   T.-P. Fries, T. Belytschko, "The extended/generalized finite element method: an overview of the method and its applications," *International Journal for Numerical Methods in Engineering*, vol. 84, no. 3, pp. 253–304, 2010.

[2]   O. C. Zienkiewicz, R. L. Taylor, J. Z. Zhu, *The finite element method: its basis and fundamentals*, 6th edition, Butterworth-Heinemann, 2005.

[3]   M. Griebel, M.A. Schweitzer, "A particle-partition of unity method for the solution of elliptic, parabolic and hyperbolic PDEs," *SIAM J. Sci. Comput.*, vol. 22, pp. 853–890, 2000.

[4]   K.-C. Kwon, S.-K. Youn, "The least-squares meshfree method for rigid-plasticity with frictional contact," *International Journal of Solids and Structures*, vol. 43, pp.7450–7841, 2006.

[5]   B. N. Rao, S. Rahman, "An efficient meshless method for fracture analysis of cracks," *Computational Mechanics*, vol. 26, pp. 398–408, 2000.

[6]   T. Belytschko, Y. Krongauz, D. Organ, M. Fleming, P. Krysl, "Meshless methods: An overview and recent developments," *Comput. Methods Appl. Mech. Engrg.*, vol. 139, pp. 3–47, 1996.

[7]   L.B. Lucy, "A numerical approach to the testing of the fission hypothesis," *Astron. J.*, vol. 82, pp. 1013–1024, 1977.

[8]   L. D. Libersky, A.G. Petscheck, T.C. Carney, J.R. Hipp, F.A. Allahdadi, "High strain Lagrangian hydrodynamics," *J. Comput. Phys.*, vol. 109, pp. 67–75, 1993.

[9]   B. Nayroles, G. Touzot, P. Villon, "Generalizing the finite element method: Diffuse approximation and diffuse elements," *Computational Mechanics*, vol. 10, pp. 307–318, 1992.

[10] T. Belytschko, Y. Y. Lu, L. Gu, "Element-free Galerkin methods," *International Journal For Numerical Methods In Engineering*, vol. 37, pp. 229–256, 1994.

[11] I. Babuška, J. M. Melenk, "The partition of unity method," International Journal for Numerical Methods In Engineering, vol. 40, pp. 727–758, 1997.

[12] S. N. Atluri, T. Zhu, "A new meshless local Petrov–Galerkin (MLPG) approach in computational mechanics," *Comput. Mech.*, vol. 22, pp. 117–127, 1998

[13] P. J. Davis, *Interpolation and approximation*, Blaisdell, London, 1963

[14] E. J. Kansa, "Multiquadrics scattered data approximation scheme with applications to computational fluid-dynamics I, surface approximations and partial derivative estimates," *Comput. Math. Appl.*, vol. 19, pp. 127–145, 1990

[15] A. Ali, S. Islam, S. Haq, "A computational meshfree technique for the numerical solution of the two-dimensional coupled Burgers' equations," *Int. J. Comput. Methods Eng. Sci. Mech.*, vol. 10, pp. 406–412, 2009.

[16] Hu, Z.-C. Li, A.-D. Cheng, "Radial basis collocation methods for elliptic boundary value problems," *Comput. Math. Appl.*, vol. 50, pp. 289–320, 2005

[17] B. Šarler, "A radial basis function collocation approach in computational fluid dynamics," *Comput. Model. Eng. Sci.*, vol. 7, pp. 185–193, 2005.

[18] B. Šarler, R. Vertnik, "Meshfree explicit local radial basis function collocation method for diffusion problems," *Comput. Math. Appl.*, vol. 51, pp. 1269–1282, 2006.

[19] C.K. Lee, X. Liu, S.C. Fan, "Local multiquadric approximation for solving boundary value problems," *Comput. Mech.*, vol. 30, pp. 396–409, 2003.

[20] G. Kosec, B. Šarler, "Local RBF collocation method for Darcy flow," *Comput. Model. Eng. Sci.*, vol. 25, no. 3, pp. 197–207, 2008.

[21] G. Fasshauer, *Solving partial differential equations by collocation with radial basis functions, surface fitting and multiresolution methods*, Nashville, USA, Vanderbilt University Press, 1997.

[22] Q. H. Qin, H. Wang, V. Kompis, *MFS with RBF for thin plate bending problems on elastic foundation. Recent Advances in Boundary Element Methods*, Manolis G D, Polyzos D, eds., New York: Springer Science, 2009, pp. 367–378.

[23] M. A. Golberg, C. S. Chen, H. Bowman, H. Power, "Some comments on the use of Radial Basis Functions in the Dual Reciprocity Method" *Computational Mechanics*, vol. 21, pp. 141–148, 1998.

[24] J. G. Wang, G. R. Liu, "A point interpolation meshless method based on radial basis functions," *International Journal for Numerical Methods in Engineering*, vol. 54, pp. 1623–1648, 2002.

[25] J. G. Wang, G. R. Liu, "On the optimal shape parameters of radial basis functions used for 2-D meshless methods," *Computer methods in applied mechanics and engineering*, vol. 191, pp. 2611–2630, 2002.

[26] A. Chiappa, P. Salvini, C. Brutti, M. E. Biancolini, "Upscaling 2D finite element analysis stress results using radial basis functions," *Computers & Structures*, vol. 220, pp. 131–143, 2019.

[27] M. D. Buhmann, *Radial Basis Functions: Theory and implementation*, Cambridge Monographs on Applied and Computational Mathematics, Cambridge University Press, 2004.

[28] M. E. Biancolini, *Fast radial basis functions for engineering applications*, Springer, 2018.

[29] S. Haykin, *Neural network: a comprehensive foundation*, 2nd edition, Prentice-Hall, Englewood Cliffs, NJ, 1999.

[30] G. Casciola, D. Lazzaro, L. B. Montefusco, S. Morigi, (2006) "Shape preserving surface reconstruction using locally anisotropic radial basis function interpolants," *Computer and Mathematics with Applications*, vol. 51, no. 8, pp. 1185–1198, 2006.

[31] M. E. Biancolini, "Mesh morphing and smoothing by means of radial basis functions (RBF): a practical example using fluent and RBF morph," in: *Handbook of research on computational science and engineering: theory and practice*. IGI Global, 2011 pp. 347–380.

[32] A. De Boer, M. S. Van der Schoot, H. Bijl, "Mesh deformation based on radial basis function interpolation," *Computers and Structures*, vol. 85, no. 11–14, pp. 784–795, 2007.

[33] M. E. Biancolini, P. Salvini, "Radial basis functions for the image analysis of deformations," in: *Computational Modelling of Objects Represented in Images: Fundamentals, Methods and Applications III Proceedings of the International Symposium*, CRC Press, 2012, pp. 361–365

[34] M. E. Biancolini, A. Chiappa, F. Giorgetti, C. Groth, U. Cella, P. Salvini, "A balanced load mapping method based on radial basis functions and fuzzy sets," *International Journal For Numerical Methods In Engineering*, vol. 115, no. 12, pp. 1411–1429, 2018.

[35] M. E. Biancolini, U. Cella, C. Groth, M. Genta, "Static aeroelastic analysis of an aircraft wind-tunnel model by means of modal RBF mesh updating," *Journal of Aerospace Engineering*, vol. 29, no. 6, 2016

[36] M. E. Biancolini, E. Costa, U. Cella, C. Groth, G. Veble, M. Andrejasic, (2016) "Glider fuselage-wing junction optimization using CFD and RBF mesh morphing," *Aircraft Engineering and Aerospace Technology*, vol. 88, pp. 740–752, 2016.

[37] C. Groth, A. Chiappa, M. E. Biancolini, "Shape optimization using structural adjoint and RBF mesh morphing," *Procedia Structural Integrity*, vol. 8, pp. 379–389, 2018

[38] P. P. Valentini, M. E. Biancolini, "Interactive sculpting using augmented-reality, mesh morphing, and force feedback: force-feedback capabilities in an augmented reality environment," *IEEE Consumer Electronics Magazine*, vol. 7, no. 2, pp. 83–90, 2018.

[39] P. B. Boyd, K. W. Gildersleeve, "Numerical experiments on the condition number of the interpolation matrices for radial basis functions," *Applied Numerical Mathematics*, vol. 61, pp. 443–459, 2011.

[40] W. Pilkey, D. Pilkey, *Peterson's stress concentration factors*, J.Wiley & Sons, 2008.

[41] R. C. J. Howland, *On the stress in the neighbourhood of a circular hole in a strip under tension*, Phil.Trans.Royal Society, London, 1930.

[42] U. Cella, M. E. Biancolini, C. Groth, A. Chiappa, D. Beltramme, "Development and validation of numerical tools for FSI analysis and structural optimization: the EU "Ribes" project status," *AIAS Congress*, Messina, Italy 2015